Two-Dimensional Electronic Spectroscopy Resolves Relative Excited State Displacements

[1]Giovanni Bressan, [1]Dale Green, [1]Garth A. Jones, [2]Ismael A. Heisler and [1,*]Stephen R. Meech

[1]School of Chemistry, Norwich Research Park, University of East Anglia, Norwich NR4 7TJ, United Kingdom

[2]Instituto de Fisica, Universidade Federal do Rio Grande do Sul, Brazil

Abstract:

Knowledge of relative displacements between potential energy surfaces (PES) is critical in spectroscopy and photochemistry. Information on displacements is encoded in vibrational coherences. Here we apply ultrafast two-dimensional electronic spectroscopy in a pump-probe half-broadband (HB2DES) geometry to probe the ground and excited state potential landscapes of cresyl violet. 2D coherence maps reveal that while the coherence amplitude of the dominant 585 cm^{-1} Raman active mode is mainly localised in ground state bleach and stimulated emission regions, a 338 cm^{-1} mode is enhanced in excited state absorption. Modelling these data with a three-level displaced harmonic oscillator model using the hierarchical equation of motion-phase matching approach (HEOM-PMA) shows that the $S_1 \leftarrow S_0$ PES displacement is greater along the 585 cm^{-1} than the 338 cm^{-1} coordinate, while $S_n \leftarrow S_1$ displacements are similar along both coordinates. HB2DES is thus a powerful tool for exploiting nuclear wavepackets to extract quantitative multidimensional, vibrational coordinate information across multiple PESs.

*corresponding author: s.meech@uea.ac.uk

The role of coherent superpositions of vibrational, vibronic or electronic states in fundamental photophysical, photochemical and photobiological processes has been thoroughly investigated by ultrafast spectroscopies.[1–7] In the past twenty years, two-dimensional electronic spectroscopy (2DES) emerged as the ideal tool for investigation of such effects in condensed phase systems, due to its ability to decongest spectra and recover rephasing (photon-echo) and non-rephasing signals.[8–13] Pump-probe 2DES is a four-wave mixing technique in which a pair of ultrashort time-ordered collinear pump pulses coherently excites electronic or vibronic transitions. Those are interrogated by a delayed, visible probe pulse which is, in the 'half-broadband (HB)' design, a compressed white-light continuum (WLC).[14,15] On top of population dynamics, the pump pair initiates nuclear wavepacket dynamics, detected as amplitude modulations during the waiting (population) time T, defined as the time interval between the second pump and the WLC probe pulses. Frequency, dephasing time, spectral position and amplitude of such oscillatory features encode information on the dynamics on the excited state potential energy surfaces (PESs).[16–20] Importantly, the amplitude of a vibrational coherence reports on the displacement between the initial and final PESs along a specific normal mode coordinate.[21–25]

We performed HB2DES on the system cresyl violet perchlorate (CV) in ethanol (EtOH). CV is a cationic oxazine dye, that has been widely studied by one-colour 2DES, leading to a wealth of data on population and coherence dynamics associated with the ground-state bleach (GSB) and stimulated emission (SE) transitions.[26–30] Utilising the extended range of the WLC probe in HB2DES enables access to higher electronic states, S_n, via excited state absorption (ESA), revealing previously inaccessible coherent dynamics. This allows us to probe displacement among higher excited states through the relative amplitude of wavepackets arising from multiple Raman active modes coupled to different electronic transitions. This ability to probe electronic and vibronic features of higher lying excited states is increasingly important. Several recent observations show that excitation of electronic states higher than S_1 leads to novel photophysical and photochemical processes not accessible by other pathways.[31–35]

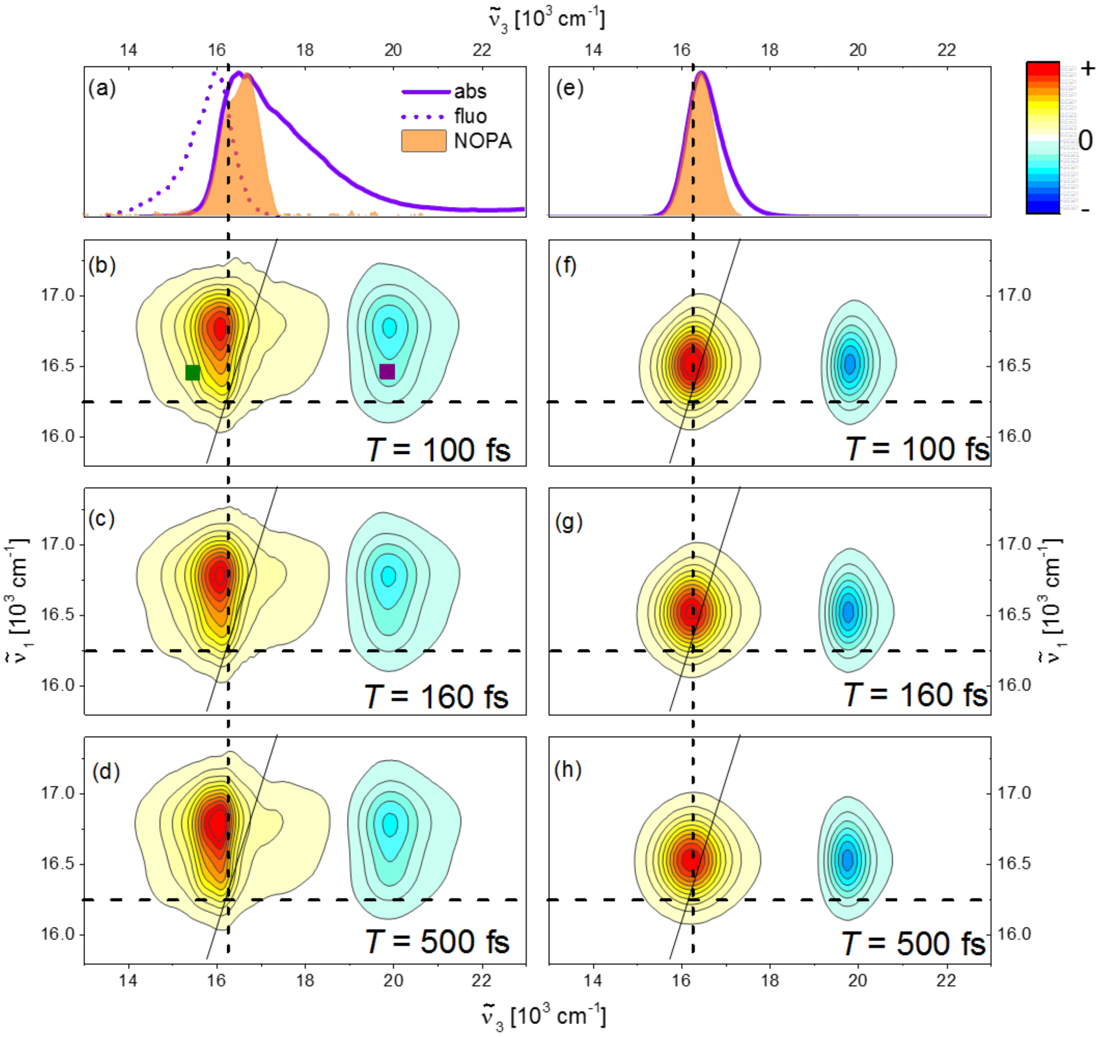

Figure 1 . (a) Normalised steady-state experimental absorption (solid) and emission (dotted) of cresyl violet (CV) in ethanol. The NOPA pump spectrum used for the HB2DES measurements is shown as a shaded orange area. The experimental absorptive 2D spectra of CV at T = 100, 160 and 500 fs are shown in (b), (c), (d) respectively. The intensity is given by 21 contour lines, positive signals are shown in yellow-orange-red and negative signals are shown in blue. All spectra are normalised to the 2DES amplitude at T = 100 fs. Dashed lines indicate the position of the 0-0 transition (16250 cm^{-1}). (e) Is the same as (a), for the simulated 2DES of CV (details of the simulation are given below and in supporting information). (f), (g), (h) Are simulated absorptive 2DES spectra of CV at T = 100, 160 and 500 fs, respectively. Dark green and purple squares indicate the coordinates at which the traces shown in Figure 2 are taken.

Experimental absorptive HB2DES spectra of CV in EtOH at waiting times T = 100, 160, 500 fs are shown in Figure 1 b, c, d. Steady state absorption and emission ($\tilde{\nu}_{exc}$ = 17000 cm^{-1}) of CV are shown in Figure 1a as violet solid and dotted lines, respectively, along with the pump spectrum employed. Dashed lines indicate the frequency of the 0-0 $S_1 \leftarrow S_0$ transition, determined by the crossing point of the normalised steady-state absorption and emission spectra at 16250 cm^{-1}. Calculated HB2DES spectra at T = 100, 160, 500 fs are shown in Figure 1 f, g, h, while the steady-state absorption and pump spectra used in the 2DES simulations are reported in Figure 1e, following the colour code of Figure 1a. The spectra in Figure 1 f-h were calculated using the hierarchical equations of motion (HEOM) method that fully accounts for solvent effects through multiple overdamped baths in combination with the equation of motion-phase matching approach (EOM-PMA), explicitly accounting for the electric fields of the pump and probe pulses, as previously described by Green *et al*.[36] Full details of the model are given in the SI.

The experimental and modelled absorptive 2DES are in very good agreement, both in terms of peak positioning and broadening, indicating that the correct Hamiltonian and bath parameters (reported in SI) are employed for the modelled spectra of CV in EtOH. The calculated steady-state absorption (to which the GSB is related) is narrower than the experimental spectrum because the model accounts for the broadening with only a single low frequency vibration coupled to the electronic transition.

Absorptive 2DES spectra present a convoluted positive GSB and SE (GSB+SE) region, matching the steady-state absorption and emission spectra, for probe ($\tilde{\nu}_3$) wavenumbers between 14000 - 18800 cm^{-1} and a negative ESA band located in the $\tilde{\nu}_3$ range 19000 - 21500 cm^{-1}. These results are in agreement with literature 2DES and visible fs transient absorption (fsTA) of CV.[26–28,37–39] 2D lineshapes display negligible evolution over the waiting time *T* (1.2 ps), suggesting that any reshaping due to spectral diffusion occurs on a timescale comparable to the ~50 fs instrument response function (IRF, shown in Figure S1). This is in agreement with the <50 fs 2DES spectral diffusion dynamics observed by Lu *et al*[28] for CV in methanol solvent.

Traces extracted from the GSB+SE and ESA regions of the absorptive 2DES spectra are shown in the SI (Figure S2). We observed a picosecond timescale SE risetime ($\tilde{\nu}_1$ = 16500; $\tilde{\nu}_3$ = 15800 cm^{-1}) which has been previously reported in a 2DES study of CV by Carbery *et al.*[27] Over the same waiting time window, the negative ESA region ($\tilde{\nu}_1$ = 16500; $\tilde{\nu}_3$ = 19900 cm^{-1}) decays with a similar timescale. Such dynamics report on the evolution within the S_1 PES and may reflect intramolecular vibrational energy redistribution (IVR) or structural dynamics, whose characterisation is beyond the scope of the present work.

The population relaxation as a function of *T* for the GSB+SE and ESA features is accompanied by strong oscillations due to coherent wavepacket dynamics. This is exemplified by the residuals of a global fit (two exponential terms, τ_1 = 350 fs, τ_2 = 5000 fs + offset) to the measured rephasing real response at two spectral points in the 2DES, marked in Figure 1b by dark green and purple squares (Figure 2).

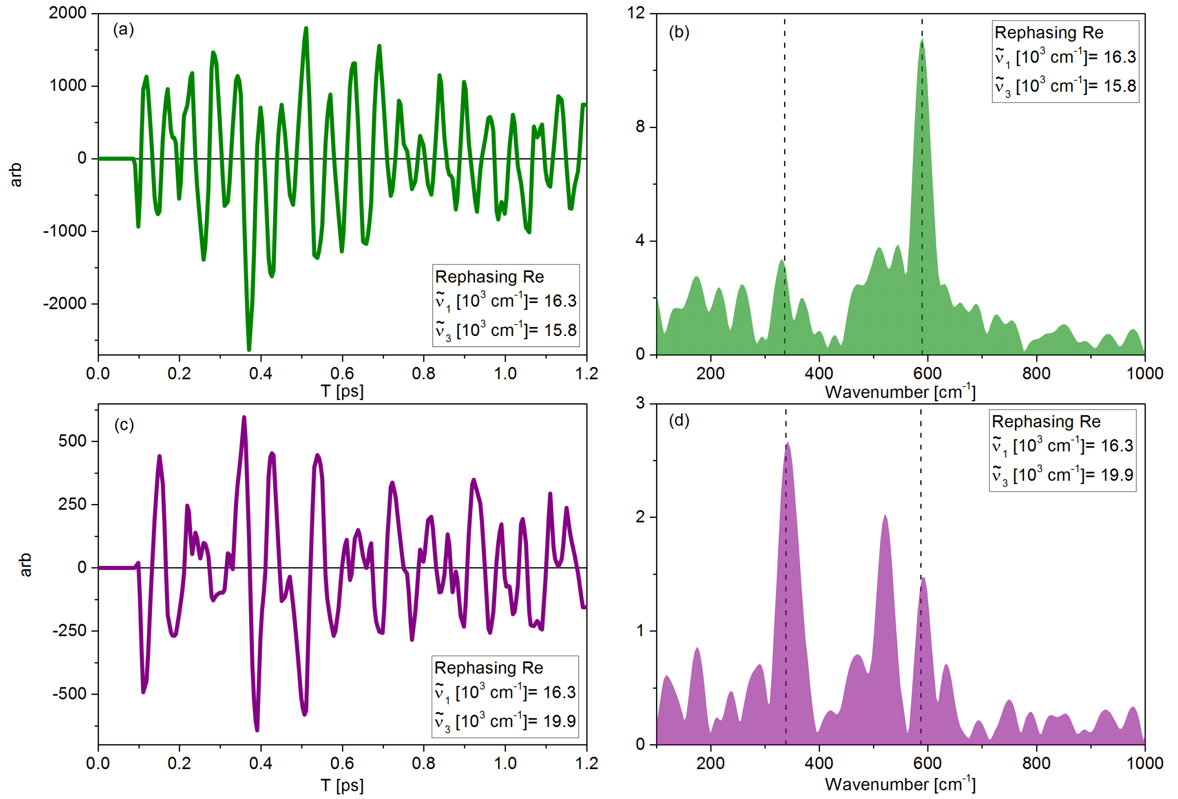

Figure 2 (a) Time-domain oscillatory residuals of the real part of the rephasing 2DES of cresyl violet, at the coordinates marked by the green square in Figure 1b. (b) Fourier transform of the residuals in (a). (c) Same as (a), at the coordinate marked by the purple square in Figure 1b. (d) Same as (b) for the oscillatory residuals shown in (c).

Figure 2a shows the residuals at excitation and detection frequencies $\tilde{\nu}_1$ = 16500 cm^{-1}; $\tilde{\nu}_3$ = 15800 cm^{-1} (GSB+SE region). The residuals show a single dominant frequency whose dephasing time outlasts the measured experimental waiting time (*T*) window of 1200 fs. After zero-padding (to the second closest power of 2) and Fourier transforming the residuals in 2a, the impulsive Raman spectrum obtained is shown in Figure 2b. This spectrum is dominated by a mode at 585 cm^{-1}, which has been reported previously as a strongly allowed, Raman active oxazine ring elongation mode.[21,28,40] Weaker contributions at 338 and 520 cm^{-1} are also present, in agreement with previous 2DES, spontaneous Resonance (RR), impulsive stimulated Raman (ISRS) and fsTA studies of CV.[21,28,38–40] The real part of the rephasing residuals over *T* at $\tilde{\nu}_1$ = 16300; $\tilde{\nu}_3$ = 19900 cm^{-1} in the ESA region are shown in Figure 2c. In contrast to the data in Figure 2a, interference between multiple frequencies with comparable amplitudes is evident. The corresponding impulsive Raman spectrum is shown in Figure 2d. Its most intense feature is a 338 cm^{-1} mode, assigned by Vogel *et al*. to a skeletal deformation,[40] which exceeds the intensity in the 585 cm^{-1} mode by 1.5 times. This mode is present in Figure 2b (GSB+SE region) but ~4 times weaker than the 585 cm^{-1} mode. Such a "reversal" of the 338 and 585 cm^{-1} relative amplitudes between the GSB+SE and the ESA regions was previously reported in a femtosecond coherence spectroscopy (FCS) study of CV by Fitzpatrick *et al*.[38]

Deeper insights into the excitation and detection frequency dependence of nuclear wavepackets can be obtained by analysing the coherence beatmaps of the two well resolved Raman active modes at 338 and 585 cm^{-1}. The objective is to resolve the origin of the striking ($\tilde{\nu}_1; \tilde{\nu}_3$) coordinate dependent amplitude reversal in the “single trace” impulsive Raman spectra reported in Figure 2 b,d. The positive and negative beatmaps of the 338 and 585 cm^{-1} modes are obtained by stacking rephasing (or nonrephasing) real and imaginary 2D spectra as a function of waiting time *T*. These are then globally fit to a multiexponential decaying function, to isolate the “slow” (ps-ns) population dynamics. The residuals of the real and imaginary global fit are then summed as $R_{Re} + \ iR_{Im}$ (where $R_{Re/Im}$ are the real or imaginary residuals matrices) to yield a complex-valued matrix which is Fourier transformed over *T*. Finally, beatmaps of specific Raman active modes are obtained by slicing along $\tilde{\nu}_T$ (*i.e.* the frequency dimension obtained by Fourier transforming over *T*) the 3D dataset at the wavenumber of the Raman active modes of interest.[13,41,42] Experimental and calculated rephasing ±338/585 cm^{-1} beatmaps are shown in Figure 3, whilst the corresponding nonrephasing data are shown in the SI (Figure S3). Rephasing and nonrephasing measured and calculated beatmaps are overlaid on contour lines indicating the experimental, or calculated, absorptive 2DES of CV at *T* = 500 fs, reproduced from Figure 1d/h.

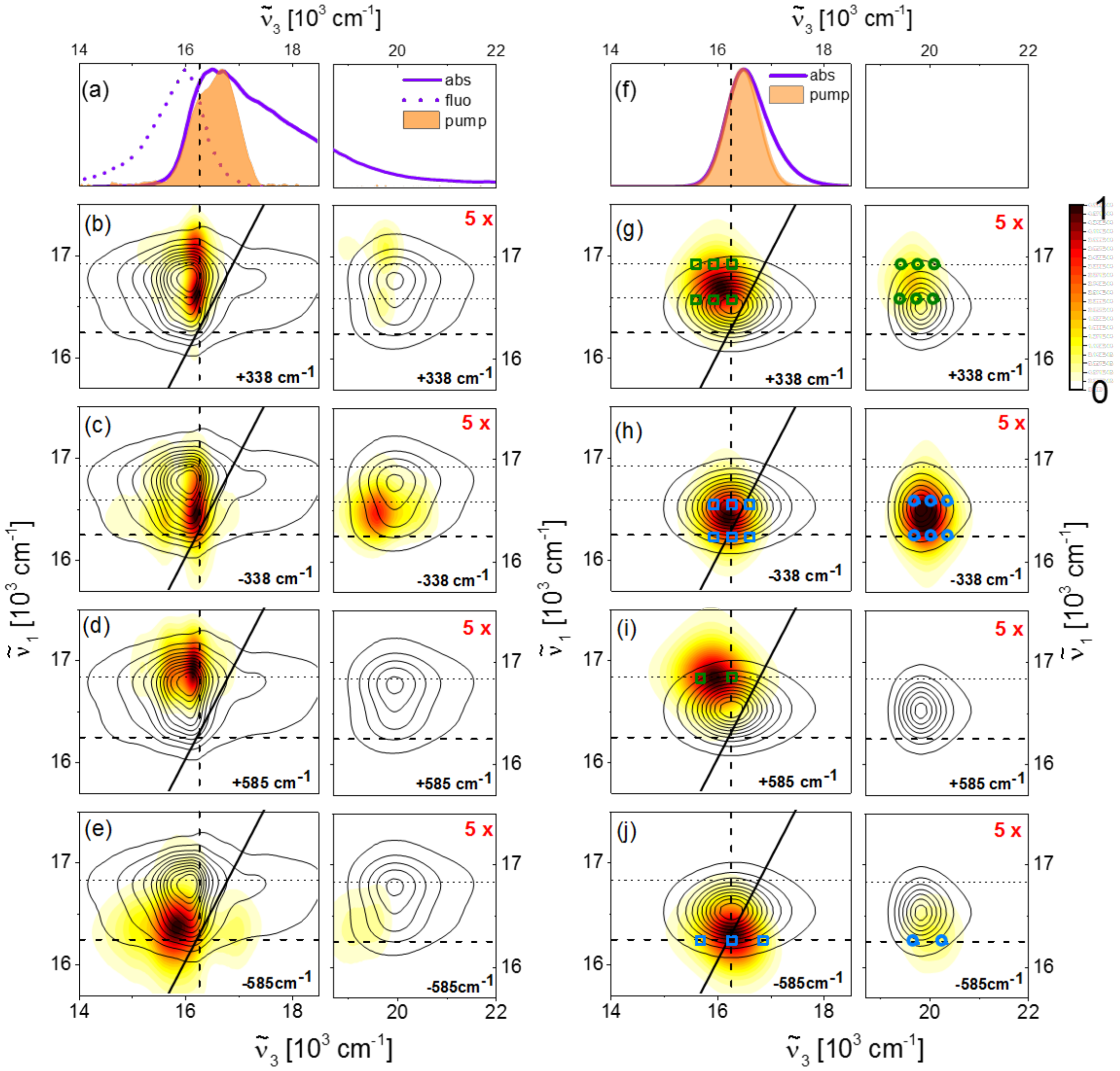

Figure 3 (a) Normalised steady-state absorption (solid) and emission (dashed) spectra of CV along with the NOPA pump spectrum. The probe axes are broken at 18400 cm^{-1} to highlight that the beatmap amplitudes are rescaled by 5x in the ESA regions. (b-c) Rephasing positive and negative beatmaps of the 338 cm^{-1} Raman active mode are shown as white-yellow-red heatmaps and are all normalised to 1. (d-e) Same as b-c for the 585 cm^{-1} Raman active mode. Contour lines showing the real part of the experimental absorptive 2D spectrum (*T* = 500 fs, reproduced from Figure 1d) are overlaid in b-e. Vertical and horizontal thick dashed lines are drawn at the 0-0 electronic transition frequency (16250 cm^{-1}) and horizontal thin dashed lines are drawn at +1, 2 quanta of vibrational excitation. (f) Shows the pump and CV steady-state absorption spectra used in the simulated 2DES of CV. (g, h) Are the same as (b, c) and (i, j) are the same as (d, e) for the simulated rephasing positive and negative beatmaps of the 338 and 585 cm^{-1} modes. Contour lines showing the real part of the calculated absorptive 2D spectrum (*T* = 500 fs, reproduced from Figure 1h) are overlaid in g-j. Green (blue) squares and circles indicate the location of positive (negative) SE and ESA double-sided Feynman diagrams contributing to the experimentally detected and calculated beatmaps, respectively.

Figure 3 shows the excitation and detection wavenumber resolved beatmap amplitudes of the rephasing positive and negative coherences due to the 338 cm^{-1} (b and c respectively) and 585 cm^{-1} (d and e) modes, compared to the steady-state absorption and emission spectra and pump spectrum (a). In Figures 3b to 3e the ESA region of the beatmaps is multiplied by a factor of five, enabling better visualization of the weaker signals detected in that region. Figures 3g to j show the ±338/±585 cm^{-1} beatmaps modelled using the steady-state absorption and pump spectra shown in Figure 3f.

The differences in the measured beatmap intensity distributions between 338 and 585 cm^{-1} modes are well reproduced by including a third electronic state in the displaced harmonic oscillator (DHO) model of Green *et al.*[36] This third state allows inclusion of S_1 to S_n ESA. The 338 cm^{-1} and 585 cm^{-1} beatmaps are modelled separately, each coupled to two baths, one for electronic dephasing and one for vibrational relaxation. Each Raman active mode is coupled to three singlet electronic states: the ground state S_0, $|g\rangle$, the first excited state S_1, $|e\rangle$, and a higher lying excited state S_n,$|f\rangle$, with energies $E_n, n = \{g, e, f\}$. The system Hamiltonian is thus,

$$H_S = |g\rangle(E_g + h_g)\langle g| + |e\rangle(E_e + h_e)\langle e| + |f\rangle(E_f + h_f)\langle f|, \tag{1}$$

with the nuclear contribution to the ground electronic state,

$$h_g = \hbar\omega_x\left(\frac{1}{2}(Q_x^2 + P_x^2) + \frac{1}{2}\right), \tag{2}$$

which assumes the mode x = {338, 585} is harmonic with coordinate Q_x, momentum P_x, and frequency ω_x. Coupling between the vibrational mode and electronic excited states translates to a displacement along the vibrational coordinate with respect to the ground state minimum of Δ_{eg}^x for S_1 and Δ_{fg}^x for S_n such that,

$$h_i = \hbar\omega_x\left(\frac{1}{2}(Q_x^2 + P_x^2) + \frac{1}{2} - \Delta_{ig}^x Q_x + \frac{1}{2}(\Delta_{ig}^x)^2\right), \tag{3}$$

where $i = \{e, f\}$ and the vibrational frequency is assumed the same for all electronic states. The last term on the right-hand side of Equation 3 corresponds to the reorganisation energy for each excited state PES. Accounting for the Stokes shift, the electronic transition frequency between S_0 and S_1, $\tilde{\nu}_{eg} = \frac{\omega_{eg}}{2\pi c} = 16250$ cm^{-1}, is taken as the crossing point between the normalised steady-state absorption and fluorescence spectra. The electronic transition frequency between S_1 and S_n is set so that the frequency of ESA maximum matches the 2D spectra in Figure 1b-d, for which $\tilde{\nu}_3$ = 19850 cm^{-1}. The displacements between ground and first excited states of CV were determined experimentally by Batignani *et al.* from pre-resonant impulsive stimulated Raman scattering (ISRS) spectroscopy as Δ_{eg}^{585} = 0.63 for the 585 cm^{-1} mode and Δ_{eg}^{338} = 0.18 for the 338 cm^{-1} mode,[21] in agreement with our experimental results, which show that the oxazine ring elongation at 585 cm^{-1} is the only Raman active mode which is strongly resonantly enhanced, thus significantly displaced, between S_0 and S_1. Excellent agreement between experimental and calculated 2D beatmaps of CV is achieved with displacements between the ground and higher excited states of Δ_{fg}^{585} = 0.73 for the 585 cm^{-1} mode and Δ_{fg}^{338} = 0.28 for 338 cm^{-1} mode. As $\Delta_{fg}^{x} = \Delta_{fe}^{x} + \Delta_{eg}^{x}$, this corresponds to an equal $S_n \leftarrow S_1$ displacement of Δ_{fe}^{x} = 0.1 for both modes. This in-turn implies that the relative displacement in ESA, $\Delta_{fe}^{x}/\Delta_{eg}^{x}$, is over 3 times larger for the 338 cm^{-1} mode (~0.5) compared to the 585 cm^{-1} mode (~0.16). This change is the origin of greater relative intensity of the 338 cm^{-1} mode beatmaps compared to the 585 cm^{-1} mode in the ESA region. These displacements are shown in the PESs diagram in Figure 4.

Next we turn to the $\tilde{\nu}_1$ dependence of the rephasing ±338 and ±585 cm^{-1} beatmaps. These are discussed in terms of the DHO model,[25,42,43] with the expected locations of specific Liouville-space pathways shown in Figure 3 g-j, and the corresponding double-sided Feynman diagrams (DSFD) shown in Figures 4b, d and in the SI (Figures S5-S8). The $\tilde{\nu}_1$ dependence of positive and negative beatmaps (Figure 3) is due to the sign of the coherence evolving during *T*.[42] To prepare an excited state vibrational wavepacket, beating with a positive sign during *T*, $|e0\rangle\langle e1|$, through a rephasing pathway, the first field-dipole interaction acts on the bra at the energy of the 0-0 electronic transition plus (at least) one quantum of vibrational energy (Figure 4b). Conversely, the rephasing negative excited state vibrational coherence pathways require $|e1\rangle\langle e0|$, with the first field-dipole interaction acting on the bra at the 0-0 electronic transition frequency (Figure 4d). Hence, signals due to rephasing +338/+585 cm^{-1} excited state coherences appear blue-shifted from the fundamental along the excitation axis by (at least) one quantum of vibrational excitation. The same argument causes the rephasing -338/-585 cm^{-1} beatmaps to be centred at the 0-0 electronic transition frequency (16250 cm^{-1}), as shown by the DSFD in Figures 4b, S6 and S8. Such an effect is apparent in both the experimental (b-e) and calculated (g-j) beatmaps shown in Figure 3. The opposite excitation frequency dependence holds for nonrephasing positive and negative pathways, as shown for the experimental and calculated nonrephasing ±338 and ±585 cm^{-1} beatmaps reported in the Supplementary Information (Figure S3).

Concerning the detection frequency dependence of the rephasing beatmaps, the amplitude of both ±338 cm^{-1} experimental (Figures 3b, c) and calculated (Figures 3g, h) beatmaps is localised on the GSB+SE region ($\tilde{\nu}_3$ =14000-17000 cm^{-1}), with weaker features appearing in the ESA. Whilst rephasing positive signals contain contributions from oscillatory GSB pathways, the calculated beatmaps confirm that SE dominates, with the peaks centred amongst SE pathways above the diagonal, as a consequence of the pump spectrum being located on the centre of the absorption band.[36,41] Conversely, rephasing negative beatmaps with no GSB contribution are selectively reporting on S_1 vibrational coherences. Thus, the intense feature in the ESA region of the experimental rephasing -338 cm^{-1} beatmap (Figure

3c) is in very good agreement with the calculations (Figure 3h) and constitutes unambiguous indication of a strong vibrational coherence in the S_1 PES of CV.

The most striking discrepancy between measured and calculated beatmaps is the double peak structure evident in the GSB+SE region of the experimental rephasing ±338 cm^{-1} beatmaps, reported in Figure 3b, c and in the experimental nonrephasing data shown in Figure S3, which are not reproduced by the DHO model. It has been shown that interference between multiple vibrational wavepackets due to harmonic[44] or anharmonic[45] couplings can introduce additional complexity into 2D beatmaps. The ~500 cm^{-1} excitation frequency separation between the peaks in the experimental ±338 cm^{-1} beatmaps could suggest coupling between the 338 cm^{-1} mode and another Raman active mode in the S_1 PES, which was not accounted for in the model.

The positive and negative experimental (Figure 3 d, e) and calculated (Figure 3 i, j) rephasing beatmaps at 585 cm^{-1} are remarkably different to those for 338 cm^{-1}. Their amplitude is mainly localised in the GSB+SE region with negligible signals detected within the ESA. Again, the selectivity of rephasing negative beatmaps for S_1 coherences allows us to assign the signals in this region of the experimental (Figure 3 e) and calculated (Figure 3 j) beatmaps to the 585 cm^{-1} vibration modulating the energy gap of the SE transition.

These results show that the combination of HB2DES measurements and their simulation with a three-level DHO model directly reveals the displacements between ground state, excited state and higher excited states, through multiple resonance Raman active vibrations. Specifically, the relative amplitude of the rephasing −338 cm^{-1} beatmap in the GSB+SE and ESA regions indicates a relative displacement ($\Delta_{fe}^{x}/\Delta_{eg}^{x}$) of ~1/2 between the $S_n \leftarrow S_1$ and $S_1 \leftarrow S_0$ transitions along this normal mode coordinate. Conversely, the relative amplitude of the rephasing −585 cm^{-1} beatmap is consistent with a relative displacement of ~1/6 between $S_n \leftarrow S_1$ but with a strongly displaced $S_1 \leftarrow S_0$. In other words, despite the $S_n \leftarrow S_1$ displacement being comparable for the 338 and 585 cm^{-1} modes, the beatmap amplitude in the ESA region is controlled by the magnitude of this displacement relative to the $S_1 \leftarrow S_0$ displacement, which determines the amplitude of the S_1 wavepacket. These results are summarised in Figure 4, where the calculated displaced harmonic S_0, S_1 and S_n PESs along the 585 (Figure 4a) and 338 cm^{-1} (Figure 4c) normal mode coordinates are shown. Superimposed are arrows indicating the four field-dipole interactions corresponding to the rephasing positive SE and rephasing negative ESA DSFDs in Figure 4b and d, respectively. These conclusions are supported by the corresponding nonrephasing data, shown in the SI (Figure S3).

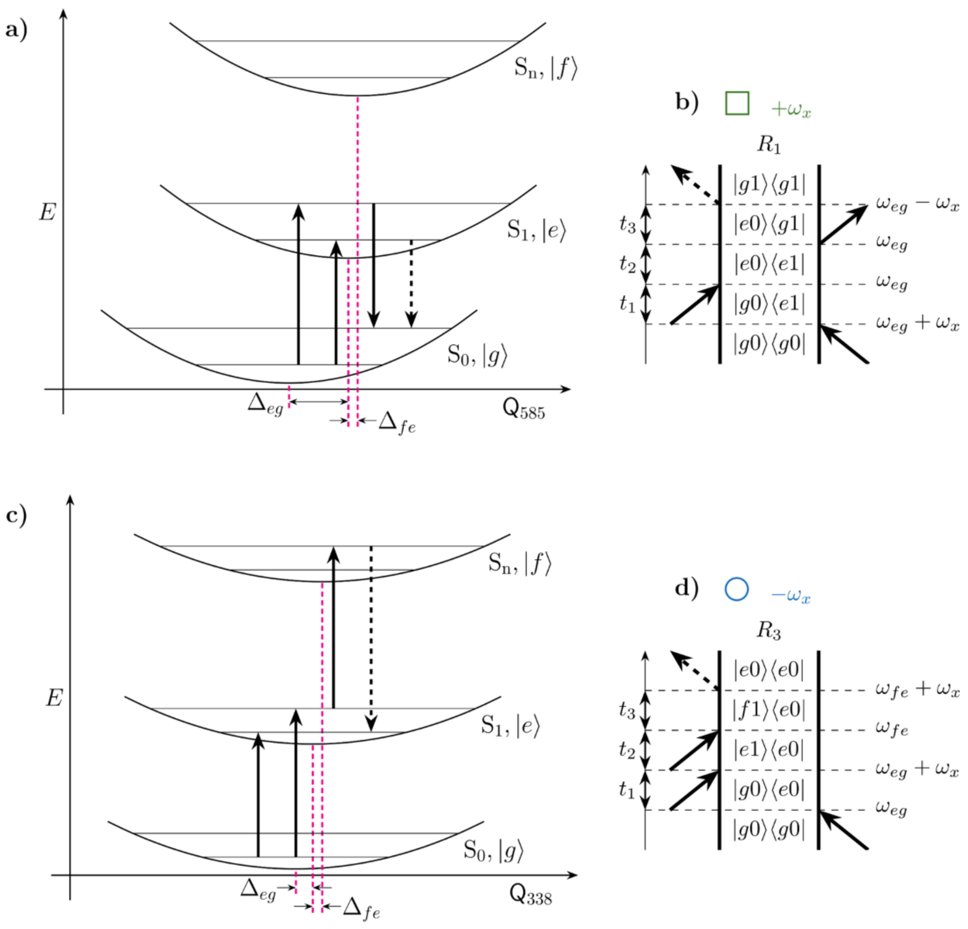

Figure 4 PESs along the 585 (a) and 338 cm^{-1} (c) normal mode coordinates. Dashed magenta vertical lines indicate the minima of the $S_{0,1,n}$ harmonic potentials, highlighting the different displacements between $S_{0,1,n}$ along the two coordinates. Vertical solid and dashed arrows represent the four field-matter interactions yielding vibrationally coherent SE (a) and ESA (c) signals with the corresponding double-sided Feynman diagrams depicted in b and d, respectively. Open squares and circles indicate vibrationally coherent SE or ESA pathways, respectively. The colour of the symbols indicates the positive (green) or negative (blue) phase of the oscillation of a double-sided Feynman diagram during *T*.

In conclusion, we reported HB2DES of CV in ethanol, where the WLC probe allows detection of coherent dynamics in both the GSB+SE and ESA regions. Striking differences in the relative amplitudes between the (338 cm^{-1}) skeletal deformation and the (585 cm^{-1}) oxazine ring elongation modes in the impulsive Raman spectra of GSB+SE and ESA spectral regions were observed. A detailed analysis of the rephasing and nonrephasing positive and negative beatmaps of these two Raman active modes revealed information on the displacements between the S_0, S_1 and S_n potential energy surfaces. We determined small (large) displacement for the 338 cm^{-1} (585 cm^{-1}) between S_0 and S_1, in agreement with literature. Conversely, the $S_n \leftarrow S_1$ transition is similarly displaced along the 338 cm^{-1} and the 585 cm^{-1} coordinates, such that a greater relative excited state displacement for the 338 cm^{-1} mode results in larger wavepacket amplitude in the ESA region. Such differences in the beatmap amplitude distributions between different Raman active modes are of particular relevance when investigating the excited state PESs of photochemically active species, in which displacements along specific vibrational coordinates may connect to the product PES.

Finally, it is worth noting the difference between HB2DES and other methods of monitoring displacements between excited state vibrational modes, such as stimulated Raman scattering in the time (ISRS) or frequency domain *e.g.* femtosecond stimulated Raman scattering, and transient 2DES spectroscopies.[46–50] Differently from these formally six-wave mixing ($\chi^{(5)}$) experiments, in which the initial actinic pulse is not involved in the preparation of ground and excited state nuclear wavepackets, coherent modulation of the $S_n \leftarrow S_1$ ESA detected in the $\chi^{(3)}$ 2DES must arise from wavepacket dynamics initiated by the pump pair. Thus, in HB2DES a null displacement along a coordinate between $S_1 \leftarrow S_0$ will prevent wavepacket dynamics in both the GSB+SE and ESA regions. Conversely, the observation of coherent dynamics in higher excited (or photochemical product) states by HB2DES directly implicates wavepacket generation initiated in the pump step.

Experimental methods:

HB2DES measurement were carried out on a 400 mOD solution (200 µm optical path static cell) of CV perchlorate (Exciton Inc.) in ethanol (EtOH). Dye and solvent were used as received. The 2DES spectrometer was previously described in detail.[51] Briefly, 10% of the output of a Ti:sapphire regenerative amplifier (Spitfire Ace, Spectra-Physics) operating at 1 kHz and 800 nm seeds a noncollinear optical parametric amplifier (NOPA, Topas White, Light Conversion). The NOPA output, (16400 cm^{-1}, ~800 nJ energy per pulse pair) is compressed by a commercial folded grism compressor (Fastlite) and a pair of pump pulses with controllable interpulse delay and relative carrier wave phase is generated in a commercial acousto-optical programmable dispersive filter (AOPDF, Dazzler, Fastlite). The coherence time is scanned, updating interpulse delay and relative phase on a shot-to-shot basis, from 0 to 95 fs in 792 as steps. A three-frame phase-cycling scheme is used to obtain real and imaginary parts of the rephasing, nonrephasing and absorptive 2D spectra.[52] Each 2D spectrum is averaged over 180 laser shots per coherence time point. The waiting time *T* is introduced by scanning the pump pair against the probe by a retroreflector mounted on a mechanical delay stage (Physik Instrumente), in 10 fs steps from 0 to 1200 fs. The white light continuum (WLC) probe is generated by focusing a small fraction of the regenerative amplifier output in a 3 mm static sapphire plate and spans 13000 - 23000 cm^{-1}. The WLC is then compressed by two pairs of dispersive mirrors (PC 1332, Ultrafast Innovations), split by a 50:50 beamsplitter and crossed at 4 degrees with the collinear pumps at the sample position. Pump(s) and probe spot sizes are 80 and 160 µm, respectively. Signal and reference are passed through a dual channel home-built prism-based spectrometer and recorded shot-to-shot by a pair of 1024 pixels CCD detectors (Stresing) synchronised to the amplifier and the AOPDF. The signal is referenced using an active noise reduction method proposed by Feng *et al.*[53] to optimise signal-to noise.[51]

Acknowledgements

The simulations presented in this paper were carried out on the High Performance Computing Cluster supported by the Research and Specialist Computing Support service at the University of East Anglia. We acknowledge support from the Engineering and Physical Sciences Research Council under Award No. EP/V00817X/1.

Supporting Information

Supporting Information Available: Instrument response function, 2DES traces, nonrephasing beatmaps, model details and double-sided Feynman diagrams.

References

(1) Johnson, P. J. M.; Farag, M. H.; Halpin, A.; Morizumi, T.; Prokhorenko, V. I.; Knoester, J.; Jansen, T. L. C.; Ernst, O. P.; Miller, R. J. D. The Primary Photochemistry of Vision Occurs at the Molecular Speed Limit. *J. Phys. Chem. B* **2017**, *121* (16), 4040–4047.

(2) Rafiq, S.; Fu, B.; Kudisch, B.; Scholes, G. D. Interplay of Vibrational Wavepackets during an Ultrafast Electron Transfer Reaction. *Nat. Chem.* **2021**, *13* (1), 70–76.

(3) Cao, J.; Cogdell, R. J.; Coker, D. F.; Duan, H.-G.; Hauer, J.; Kleinekathöfer, U.; Jansen, T. L. C.; Mančal, T.; Miller, R. J. D.; Ogilvie, J. P.; et al. Quantum Biology Revisited. *Sci. Adv.* **2020**, *6* (14), 4888.

(4) Fuller, F. D.; Pan, J.; Gelzinis, A.; Butkus, V.; Senlik, S. S.; Wilcox, D. E.; Yocum, C. F.; Valkunas, L.; Abramavicius, D.; Ogilvie, J. P. Vibronic Coherence in Oxygenic Photosynthesis. *Nat. Chem.* **2014**, *6* (8), 706–711.

(5) Sardjan, A. S.; Roy, P.; Danowski, W.; Bressan, G.; Nunes dos Santos Comprido, L.; Browne, W. R.; Feringa, B. L.; Meech, S. R. Ultrafast Excited State Dynamics in a First Generation Photomolecular Motor. *ChemPhysChem* **2020**, *21* (7), 594–599.

(6) Bressan, G.; Jirasek, M.; Roy, P.; Anderson, H. L.; Meech, S. R.; Heisler, I. A. Population and Coherence Dynamics in Large Conjugated Porphyrin Nanorings. *Chem. Sci.* **2022**, *13* (33), 9624–9636.

(7) Rafiq, S.; Weingartz, N. P.; Kromer, S.; Castellano, F. N.; Chen, L. X. Spin–Vibronic Coherence Drives Singlet–Triplet Conversion. *Nature* **2023**, *620* (7975), 776–781.

(8) Oliver, T. A. A. Recent Advances in Multidimensional Ultrafast Spectroscopy. *R. Soc. Open Sci.* **2018**, *5* (1), 171425.

(9) Gelzinis, A.; Augulis, R.; Butkus, V.; Robert, B.; Valkunas, L. Two-Dimensional Spectroscopy for Non-Specialists. *Biochim. Biophys. Acta - Bioenerg.* **2019**, *1860* (4), 271–285.

(10) Meneghin, E.; Volpato, A.; Cupellini, L.; Bolzonello, L.; Jurinovich, S.; Mascoli, V.; Carbonera, D.; Mennucci, B.; Collini, E. Coherence in Carotenoid-to-Chlorophyll Energy Transfer. *Nat. Commun.* **2018**, *9* (1), 3160.

(11) Kim, T.; Lin, C.; Schultz, J. D.; Young, R. M.; Wasielewski, M. R. π-Stacking-Dependent Vibronic Couplings Drive Excited-State Dynamics in Perylenediimide Assemblies. *J. Am. Chem. Soc.*

2022, *144* (25), 11386–11396.

(12) Bressan, G.; Cammidge, A. N.; Jones, G. A.; Heisler, I. A.; Gonzalez-Lucas, D.; Remiro-Buenamañana, S.; Meech, S. R. Electronic Energy Transfer in a Subphthalocyanine–Zn Porphyrin Dimer Studied by Linear and Nonlinear Ultrafast Spectroscopy. *J. Phys. Chem. A* **2019**, *123* (27), 5724–5733.

(13) Bressan, G.; Green, D.; Chan, Y.; Bulman Page, P. C.; Jones, G. A.; Meech, S. R.; Heisler, I. A. One- to Two-Exciton Transitions in Perylene Bisimide Dimer Revealed by Two-Dimensional Electronic Spectroscopy. *J. Phys. Chem. A* **2019**, *123* (8), 1594–1601.

(14) Tekavec, P. F.; Myers, J. a; Lewis, K. L. M.; Ogilvie, J. P. Two-Dimensional Electronic Spectroscopy with a Continuum Probe. *Opt. Lett.* **2009**, *34* (9), 1390.

(15) Seiler, H.; Palato, S.; Schmidt, B. E.; Kambhampati, P. Simple Fiber-Based Solution for Coherent Multidimensional Spectroscopy in the Visible Regime. *Opt. Lett.* **2017**, *42* (3), 643.

(16) Brazard, J.; Bizimana, L. A.; Gellen, T.; Carbery, W. P.; Turner, D. B. Experimental Detection of Branching at a Conical Intersection in a Highly Fluorescent Molecule. *J. Phys. Chem. Lett.* **2016**, *7* (1), 14–19.

(17) Schultz, J. D.; Shin, J. Y.; Chen, M.; O'Connor, J. P.; Young, R. M.; Ratner, M. A.; Wasielewski, M. R. Influence of Vibronic Coupling on Ultrafast Singlet Fission in a Linear Terrylenediimide Dimer. *J. Am. Chem. Soc.* **2021**, *143* (4), 2049–2058.

(18) Farag, M. H.; Jansen, T. L. C.; Knoester, J. Probing the Interstate Coupling near a Conical Intersection by Optical Spectroscopy. *J. Phys. Chem. Lett.* **2016**, *7* (17), 3328–3334.

(19) Scholes, G. D.; Fleming, G. R.; Chen, L. X.; Aspuru-Guzik, A.; Buchleitner, A.; Coker, D. F.; Engel, G. S.; van Grondelle, R.; Ishizaki, A.; Jonas, D. M.; et al. Using Coherence to Enhance Function in Chemical and Biophysical Systems. *Nature* **2017**, *543* (7647), 647–656.

(20) Albrecht, A. C. On the Theory of Raman Intensities. *J. Chem. Phys.* **1961**, *34* (5), 1476–1484.

(21) Batignani, G.; Sansone, C.; Ferrante, C.; Fumero, G.; Mukamel, S.; Scopigno, T. Excited-State Energy Surfaces in Molecules Revealed by Impulsive Stimulated Raman Excitation Profiles. *J. Phys. Chem. Lett.* **2021**, *12* (38), 9239–9247.

(22) Batignani, G.; Mai, E.; Fumero, G.; Mukamel, S.; Scopigno, T. Absolute Excited State Molecular Geometries Revealed by Resonance Raman Signals. *Nat. Commun.* **2022**, *13* (1), 7770.

(23) Mukamel, S. *Principles of Nonlinear Optical Spectroscopy*; Oxford University Press: New York, 1995.

(24) Dean, J. C.; Scholes, G. D. Coherence Spectroscopy in the Condensed Phase: Insights into Molecular Structure, Environment, and Interactions. *Acc. Chem. Res.* **2017**, *50* (11), 2746–2755.

(25) Butkus, V.; Zigmantas, D.; Valkunas, L.; Abramavicius, D. Vibrational vs. Electronic Coherences in 2D Spectrum of Molecular Systems. *Chem. Phys. Lett.* **2012**, *545*, 40–43.

(26) Heisler, I. A.; Moca, R.; Camargo, F. V. A.; Meech, S. R. Two-Dimensional Electronic Spectroscopy Based on Conventional Optics and Fast Dual Chopper Data Acquisition. *Rev. Sci. Instrum.* **2014**, *85* (6), 063103.

(27) Carbery, W. P.; Pinto-Pacheco, B.; Buccella, D.; Turner, D. B. Resolving the Fluorescence Quenching Mechanism of an Oxazine Dye Using Ultrabroadband Two-Dimensional Electronic Spectroscopy. *J. Phys. Chem. A* **2019**, *123* (24), 5072–5080.

(28) Lu, J.; Lee, Y.; Anna, J. M. Extracting the Frequency-Dependent Dynamic Stokes Shift from Two-Dimensional Electronic Spectra with Prominent Vibrational Coherences. *J. Phys. Chem. B* **2020**, *124* (40), 8857–8867.

(29) Spokoyny, B.; Koh, C. J.; Harel, E. Stable and High-Power Few Cycle Supercontinuum for 2D Ultrabroadband Electronic Spectroscopy. *Opt. Lett.* **2015**, *40* (6), 1014–1017.

(30) Turner, D. B.; Wilk, K. E.; Curmi, P. M. G.; Scholes, G. D. Comparison of Electronic and Vibrational Coherence Measured by Two-Dimensional Electronic Spectroscopy. *J. Phys. Chem. Lett.* **2011**, *2* (15), 1904–1911.

(31) Sotome, H.; Nagasaka, T.; Une, K.; Morikawa, S.; Katayama, T.; Kobatake, S.; Irie, M.; Miyasaka, H. Cycloreversion Reaction of a Diarylethene Derivative at Higher Excited States Attained by Two-Color, Two-Photon Femtosecond Pulsed Excitation. *J. Am. Chem. Soc.* **2017**, *139* (47), 17159–17167.

(32) Burns, K. H.; Elles, C. G. Ultrafast Dynamics of a Molecular Switch from Resonance Raman Spectroscopy: Comparing Visible and UV Excitation. *J. Phys. Chem. A* **2022**, *126* (35), 5932–5939.

(33) Brusar, V.; Forjan, M.; Ljubić, I.; Alešković, M.; Becker, K.; Vdović, S. Ultrafast Photoelimination of Nitrogen from Upper Excited States of Diazoalkanes and the Fate of Carbenes Formed in the Reaction. *J. Org. Chem.* **2023**, *88* (7), 4286–4300.

(34) Yoshioka, D.; Fukuda, D.; Kobayashi, Y. Green and Far-Red-Light Induced Electron Injection from Perylene Bisimide to Wide Bandgap Semiconductor Nanocrystals with Stepwise Two-Photon Absorption Process. *Nanoscale* **2021**, *13* (3), 1823–1831.

(35) Miyasaka, H.; Ito, S.; Sotome, H. Reaction Dynamics of Molecules in Highly Electronically Excited States Attained by Multiphoton and Multiple Excitation Methods. *Pure Appl. Chem.* **2023**, *95* (8), 921–929.

(36) Green, D.; V. A. Camargo, F.; Heisler, I. A.; Dijkstra, A. G.; Jones, G. A. Spectral Filtering as a Tool for Two-Dimensional Spectroscopy: A Theoretical Model. *J. Phys. Chem. A* **2018**, *122* (30), 6206–6213.

(37) Ma, X.; Dostál, J.; Brixner, T. Broadband 7-Fs Diffractive-Optic-Based 2D Electronic Spectroscopy Using Hollow-Core Fiber Compression. *Opt. Express* **2016**, *24* (18), 20781.

(38) Fitzpatrick, C.; Odhner, J. H.; Levis, R. J. Spectral Signatures of Ground- and Excited-State Wavepacket Interference after Impulsive Excitation. *J. Phys. Chem. A* **2020**, *124* (34), 6856–6866.

(39) Rafiq, S.; Scholes, G. D. Slow Intramolecular Vibrational Relaxation Leads to Long-Lived Excited-State Wavepackets. *J. Phys. Chem. A* **2016**, *120* (34), 6792–6799.

(40) Vogel, E.; Gbureck, A.; Kiefer, W. Vibrational Spectroscopic Studies on the Dyes Cresyl Violet and Coumarin 152. *J. Mol. Struct.* **2000**, *550–551*, 177–190.

(41) de A. Camargo, F. V.; Grimmelsmann, L.; Anderson, H. L.; Meech, S. R.; Heisler, I. A. Resolving Vibrational from Electronic Coherences in Two-Dimensional Electronic Spectroscopy: The Role of the Laser Spectrum. *Phys. Rev. Lett.* **2017**, *118* (3), 033001.

(42) V. A. Camargo, F.; L. Anderson, H.; R. Meech, S.; A. Heisler, I. Full Characterization of Vibrational Coherence in a Porphyrin Chromophore by Two-Dimensional Electronic Spectroscopy. *J. Phys. Chem. A* **2014**, *119* (1), 95–101.

(43) Butkus, V.; Valkunas, L.; Abramavicius, D. Molecular Vibrations-Induced Quantum Beats in

Two-Dimensional Electronic Spectroscopy. *J. Chem. Phys.* **2012**, *137* (4), 44513.

(44) Schultz, J. D.; Kim, T.; O'Connor, J. P.; Young, R. M.; Wasielewski, M. R. Coupling between Harmonic Vibrations Influences Quantum Beating Signatures in Two-Dimensional Electronic Spectra. *J. Phys. Chem. C* **2022**, *126* (1), 120–131.

(45) Zhu, R.; Zou, J.; Wang, Z.; Chen, H.; Weng, Y. Electronic State-Resolved Multimode-Coupled Vibrational Wavepackets in Oxazine 720 by Two-Dimensional Electronic Spectroscopy. *J. Phys. Chem. A* **2020**, *124* (45), 9333–9342.

(46) Hall, C. R.; Conyard, J.; Heisler, I. A.; Jones, G.; Frost, J.; Browne, W. R.; Feringa, B. L.; Meech, S. R. Ultrafast Dynamics in Light-Driven Molecular Rotary Motors Probed by Femtosecond Stimulated Raman Spectroscopy. *J. Am. Chem. Soc.* **2017**, *139* (21), 7408–7414.

(47) Batignani, G.; Ferrante, C.; Scopigno, T. Accessing Excited State Molecular Vibrations by Femtosecond Stimulated Raman Spectroscopy. *J. Phys. Chem. Lett.* **2020**, *11* (18), 7805–7813.

(48) Kuramochi, H.; Takeuchi, S.; Tahara, T. Femtosecond Time-Resolved Impulsive Stimulated Raman Spectroscopy Using Sub-7-Fs Pulses: Apparatus and Applications. *Rev. Sci. Instrum.* **2016**, *87* (4), 043107.

(49) Liebel, M.; Kukura, P. Broad-Band Impulsive Vibrational Spectroscopy of Excited Electronic States in the Time Domain. *J. Phys. Chem. Lett.* **2013**, *4* (8), 1358–1364.

(50) Mandal, A.; Schultz, J. D.; Wu, Y.-L.; Coleman, A. F.; Young, R. M.; Wasielewski, M. R. Transient Two-Dimensional Electronic Spectroscopy: Coherent Dynamics at Arbitrary Times along the Reaction Coordinate. *J. Phys. Chem. Lett.* **2019**, *10* (13), 3509–3515.

(51) Bressan, G.; Heisler, I. A.; Greetham, G. M.; Edmeades, A.; Meech, S. R. Half-Broadband Two-Dimensional Electronic Spectroscopy with Active Noise Reduction. *Opt. Express* **2023**, *31* (25), 42687.

(52) Zhang, Z.; Wells, K. L.; Hyland, E. W. J.; Tan, H.-S. Phase-Cycling Schemes for Pump–Probe Beam Geometry Two-Dimensional Electronic Spectroscopy. *Chem. Phys. Lett.* **2012**, *550*, 156–161.

(53) Feng, Y.; Vinogradov, I.; Ge, N.-H. General Noise Suppression Scheme with Reference Detection in Heterodyne Nonlinear Spectroscopy. *Opt. Express* **2017**, *25* (21), 26262.

TOC figure